

## Crosswind effects on high-sided road vehicles with and without movement

Bin Wang<sup>1a</sup>, You-Lin Xu<sup>\*1</sup>, Le-Dong Zhu<sup>2b</sup> and Yong-Le Li<sup>3c</sup>

<sup>1</sup>Department of Civil and Environmental Engineering, The Hong Kong Polytechnic University, Hong Kong, China

<sup>2</sup>State Key Laboratory of Disaster Reduction in Civil Engineering, Tongji University, Shanghai, China

<sup>3</sup>Department of Bridge Engineering, Southwest Jiaotong University, Chengdu, China

(Received November 24, 2012, Revised October 15, 2013, Accepted October 26, 2013)

**Abstract.** The safety of road vehicles on the ground in crosswind has been investigated for many years. One of the most important fundamentals in the safety analysis is aerodynamic characteristics of a vehicle in crosswind. The most common way to study the aerodynamic characteristics of a vehicle in crosswind is wind tunnel tests to measure the aerodynamic coefficients and/or pressure coefficients of the vehicle. Due to the complexity of wind tunnel test equipment and procedure, the features of flow field around the vehicle are seldom explored in a wind tunnel, particularly for the vehicle moving on the ground. As a complementary to wind tunnel tests, the numerical method using computational fluid dynamics (CFD) can be employed as an effective tool to explore the aerodynamic characteristics of as well as flow features around the vehicle. This study explores crosswind effects on a high-sided lorry on the ground with and without movement through CFD simulations together with wind tunnel tests. Firstly, the aerodynamic forces on a stationary lorry model are measured in a wind tunnel, and the results are compared with the previous measurement results. The CFD with unsteady RANS method is then employed to simulate wind flow around and wind pressures on the stationary lorry. The numerical aerodynamic forces are compared with the wind tunnel test results. Furthermore, the same CFD method is extended to investigate the moving vehicle on the ground in crosswind. The results show that the CFD results match with wind tunnel test results and the current way using aerodynamic coefficients from a stationary vehicle in crosswind is acceptable. The CFD simulation can provide more insights on flow field and pressure distribution which are difficult to be obtained by wind tunnel tests.

**Keywords:** crosswind effects; road vehicles; aerodynamic characteristics; stationary and moving vehicle; wind tunnel tests; computational fluid dynamics simulation

### 1. Introduction

Baker and Reynolds (1992) conducted a post-disaster investigation on wind-induced road vehicle accidents after a storm in UK and reported that over 400 accidents occurred during the

---

\*Corresponding author, Chair Professor, E-mail: [ceylxu@polyu.edu.hk](mailto:ceylxu@polyu.edu.hk)

<sup>a</sup> Ph. D. Student, E-mail: [b.wang@connect.polyu.hk](mailto:b.wang@connect.polyu.hk)

<sup>b</sup> Professor, E-mail: [ledong@tongji.edu.cn](mailto:ledong@tongji.edu.cn)

<sup>c</sup> Professor, E-mail: [lele@swjtu.edu.cn](mailto:lele@swjtu.edu.cn)

storm and high-sided vehicles accounted for most of them. The safety of road vehicles on the ground in crosswind has been actively investigated since then (Baker 1986, Xu and Guo 2003, Snæbjörnsson *et al.* 2007, Proppe and Wetzel 2010, Kwon *et al.* 2011, Kim *et al.* 2011). One of the most important fundamentals in the safety analysis is aerodynamic characteristics of a vehicle in crosswind. The most common way to obtain the aerodynamic characteristics of a moving vehicle in crosswind is to carry out wind tunnel tests based on the following understanding.

As illustrated in Fig. 1(a), a lorry is moving on the ground with a velocity  $\mathbf{u}_v$ . Wind blows perpendicular to the vehicle with a velocity of  $\mathbf{u}_w$ . If the reference coordinate system is fixed on the lorry rather than on the ground as shown in Fig. 1(b), the moving velocity of the ground  $\mathbf{u}_{gv}$ , the velocity of upcoming wind  $\mathbf{u}_{wv}$  and its yaw angle  $\alpha$  become

$$\mathbf{u}_{gv} = -\mathbf{u}_v; \mathbf{u}_{wv} = \mathbf{u}_w - \mathbf{u}_v; \alpha = \arctan\left(\frac{|\mathbf{u}_w|}{|\mathbf{u}_v|}\right) \quad (1)$$

The right ways to obtain the aerodynamic characteristics of a vehicle are therefore either to test the aerodynamics of the moving vehicle ( $\mathbf{u}_v$ ) under perpendicular cross winds ( $\mathbf{u}_w$ ) or to measure the aerodynamics of the stationary vehicle under yawed cross winds ( $\mathbf{u}_{wv}$ ,  $\alpha$ ) with the movement of the ground ( $\mathbf{u}_{gv}$ ). These two methods are called the moving vehicle methods in this paper. However, it is not easy to realize the movement of a vehicle ( $\mathbf{u}_v$ ) or the movement of the ground ( $\mathbf{u}_{gv}$ ) in a wind tunnel. An approximate way is to neglect the relative motion between the vehicle and the ground and just measure the aerodynamics of the stationary vehicle under the yawed cross winds ( $\mathbf{u}_{wv}$ ,  $\alpha$ ). This approximation is the commonly-used way called the stationary vehicle method.

In the safety analysis of high-sided road vehicles (Baker 1988), the aerodynamic coefficients were measured in a wind tunnel using the stationary vehicle method. Coleman and Baker (1990) further carried out wind tunnel tests to measure the aerodynamic coefficients of a high-sided articulated tractor-trailer, in which the pressures were also measured for several surface points and oil flow was utilized to observe the surface flow. Afterwards, they conducted more tests to consider the influence of turbulence, wind fence, and atmospheric boundary layer on the same high-sided road vehicle (Coleman and Baker 1992, Coleman and Baker 1994). On the other hand, Howell *et al.* (1996) undertook a full scale wind tunnel test on a Rover 800 saloon car under crosswind with a yaw angle range from  $-20^\circ$  to  $20^\circ$ . The pressure distribution over the car surface was also measured. The distribution of side force and yawing moment components were derived from the pressure distribution. Passmore *et al.* (2001) measured the aerodynamic forces on a simplified car-type bluff body with the upcoming wind disturbed. Petzäll *et al.* (2008) studied the aerodynamic properties of high-sided coaches in a wind tunnel. In the wind tunnel tests of Gohlke *et al.* (2010), a min-van type vehicle was yawed to an angle of  $-30^\circ$ . The particle image velocimetry (PIV) was employed to observe the flow feature on a fixed plane parallel to the rear end of the vehicle model. Although it is a challenging task to model a moving vehicle in a wind tunnel, Humphreys and Baker (1992) conducted such kind of tests. It was found that the effect of vehicle movement was obvious at low yaw angles.

Due to the complex test equipment and processing procedure required, the information from wind tunnel tests is always very limited on the features of flow field around a vehicle. In order to have an in-deep understanding of vehicle aerodynamics, the numerical simulation using computational fluid dynamics (CFD) are employed as a complement way of the wind tunnel test. CFD is commonly used in the prediction of drag force of a moving vehicle in vehicle

aerodynamics but cross wind effects are not taken into consideration. Han (1989) simulated the flow around an Ahmed's vehicle-like body by solving the Reynolds-averaged Navier-Stokes (RANS) equations. Most of the essential features of the flow around the body were predicted including the formation of trailing vortices and the reverse flow region from separation. Krajnovic and Davidson (2003) used the large eddy simulation (LES) method to model the flow around a simplified bus moving on the ground. Sharma *et al.* (2008) using the CFD package CFX to study the drag reduction of an intercity bus. Tsubokura *et al.* (2009) also simulated the flow around a sedan using LES method. Guilmineau and Chometon (2009) modeled the steady flow characteristics of a square back test model using the RANS method. For the aerodynamics of a vehicle under cross winds, Hargreaves and Morvan (2008) simulated the aerodynamic forces of a high-sided vehicle under different wind yaw angles using the unsteady RANS method.

In the application of CFD technique to vehicle aerodynamics, one of the most important issues is the selection of turbulence model. The common modeling methods for turbulence are the steady RANS, unsteady RANS, LES, and the hybrid method between RANS and LES. LES and the hybrid method have a better capacity of simulating the turbulence. Although RANS could not be used to capture the turbulence in high precision compared with LES and the hybrid method, it needs less computational efforts to obtain the averaged flow characteristics, acceptable in engineering application. Another issue of using CFD technique is the validation of numerical results. Since there are many open doors left for the users to select turbulence model and grid meshing, the results of CFD from different users may be different. Therefore, the results of CFD should be carefully treated, for which the results from wind tunnel tests are often utilized for validation.

Both wind tunnel test and CFD have their own limitations. In this study, wind tunnel test and CFD are combined together to explore the crosswind effects of a high-sided lorry with and without movement on the ground systematically. Firstly, the aerodynamic forces of the stationary lorry are measured in a wind tunnel. Then, the CFD with the unsteady RANS method is employed to simulate the flow around the stationary vehicle at different yaw angles, in which the SST  $k-\omega$  turbulence model is used. Appropriate meshing and time step are obtained through the comparison of different schemes. The simulated aerodynamic coefficients are validated against the wind tunnel test results. The flow field features and the surface pressure coefficient distributions over the vehicle are presented in detail. Furthermore, the numerical method is expanded to model the moving lorry on the ground, and the results are compared with those from the stationary vehicle.

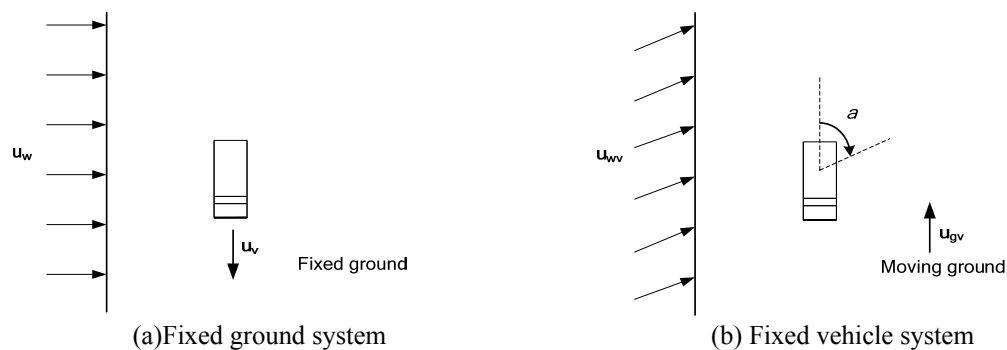


Fig. 1 Vehicle moving on the ground

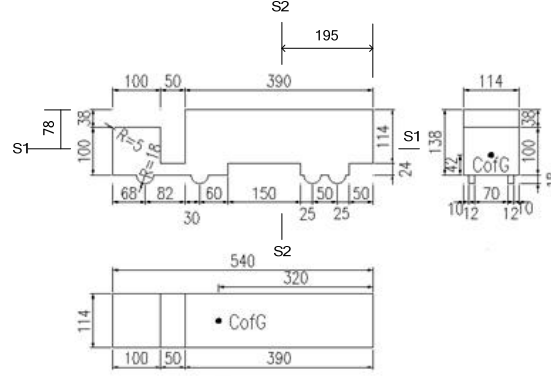


Fig. 2 Vehicle Model (unit: mm)

## 2. Wind tunnel test results

An articulated high-sided lorry with a scale of 1:25 is selected as the testing vehicle model. The geometric sizes of the vehicle model are shown in Fig. 2. The total height, width and length of the vehicle model are 0.156m, 0.114m and 0.54m, respectively. The aerodynamic force measurements are carried out in the TJ-1 wind tunnel of the State Key Laboratory for Disaster Reduction in Civil Engineering at Tongji University in China. During testing, both the models of the lorry and ground are fixed without any movement with reference to the wind tunnel. Different yaw angles of wind are realized by rotating the turntable. The Reynolds number is about  $1.13 \times 10^5$  in terms of the height of lorry. The details of the testing process could be found in Zhu *et al.* (2012).

The aerodynamic forces of the vehicle are illustrated as in Fig. 3.  $X$ ,  $Y$ ,  $Z$  are the three axes of the Cartesian coordinate system. The coordinate system is fixed on the lorry with the origin located at its gravity center. The positive  $Y$ -axis is vertical to the ground with upward direction. The positive  $Z$ -axis points from the tail to the head of the vehicle in its central symmetric vertical plane. The positive  $X$ -axis is perpendicular to the  $YZ$  plane with a right hand rule. In the figure, three aerodynamic forces and three aerodynamic moments are defined. Side force  $F_S$ , lift force  $F_L$  and drag force  $F_D$  are along the  $X$ ,  $Y$ , and  $Z$  axes, respectively. Side force drives the vehicle to sideslip. Lift force impels the vehicle to depart from the ground. Drag force impedes the movement of the vehicle. Pitching moment  $M_P$ , yawing moment  $M_Y$  and rolling moment  $M_R$  are defined as rotations around the  $X$ ,  $Y$ , and  $Z$  axes, respectively. The yawing angle  $\alpha$  is the angle between the direction of upcoming wind and the longitude axis of the vehicle ( $Z$ -axis). Corresponding to the aerodynamic forces and moments, six non-dimensional aerodynamic coefficients are presented as follows

$$C_L = \frac{F_L}{qA}; C_D = \frac{F_D}{qA}; C_S = \frac{F_S}{qA} \quad (2)$$

$$C_P = \frac{M_P}{qAL}; C_Y = \frac{M_Y}{qAL}; C_R = \frac{M_R}{qAL} \quad (3)$$

$$q = 0.5\rho U^2 \quad (4)$$

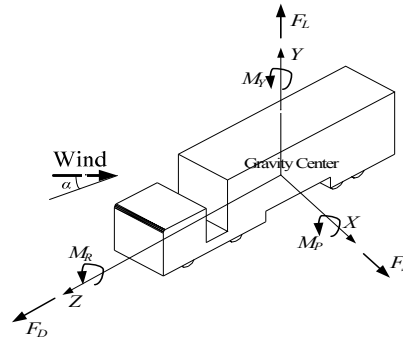


Fig. 3 Aerodynamic forces and moments of the lorry

where  $C_L$ ,  $C_D$  and  $C_S$  are the lift coefficient, drag coefficient and side force coefficient, respectively;  $C_P$ ,  $C_Y$ ,  $C_R$  are the pitching moment coefficient, yawing moment coefficient and rotating moment coefficient, respectively;  $q$  is the dynamic pressure of air;  $\rho$  is the air density;  $U$  is the upcoming wind velocity;  $L$  is the length of the vehicle; and  $A$  is the frontal project area of the vehicle without wheels and it refers to the project area in the  $X$ - $Y$  plane in Fig. 3.

Aerodynamic force coefficients at the four yaw angles of  $0^\circ$ ,  $30^\circ$ ,  $60^\circ$  and  $90^\circ$  are plotted in Fig. 4. It can be seen that the side coefficient increases with the increasing yaw angle. The lift coefficient and pitching moment coefficient increase first and decrease late with a maximum value around  $30^\circ$ . The drag coefficient decreases first and increases late with a minimum value around  $30^\circ$ . The yawing moment coefficient decreases with the yaw angle. The rotating moment decrease first and become flat beyond  $60^\circ$ . Baker and his colleagues measured the aerodynamic coefficients of a similar lorry in low turbulence (Baker 1988, Coleman and Baker 1990). The Reynolds numbers of the two wind tunnel tests they carried out are about  $2.4 \times 10^5$  and  $8.5 \times 10^4$  in terms of the height of lorry. The absolute maximum differences of aerodynamic coefficients obtained from the three tests are listed in Table 1 for different yaw angles. In most cases, the differences are not very large. The absolute maximum differences for the side coefficient, lift coefficient, drag coefficient, yawing moment coefficient, pitching moment coefficient and the rotating moment coefficient are 0.82, 1.56, 0.24, 0.48, 0.27 and 0.36, respectively, most of which occur at  $90^\circ$  yaw angle.

Table 1 Absolute maximum differences of aerodynamic coefficients from three tests

Yaw angle( $^\circ$ )	$D_{\max}(C_S)$	$D_{\max}(C_L)$	$D_{\max}(C_D)$	$D_{\max}(C_P)$	$D_{\max}(C_Y)$	$D_{\max}(C_R)$
0	0.29	0.23	0.23	0.03	0.07	0.02
30	0.82	0.40	0.24	0.08	0.14	0.15
60	0.51	1.30	0.04	0.33	0.27	0.31
90	0.81	1.56	0.16	0.48	0.27	0.36

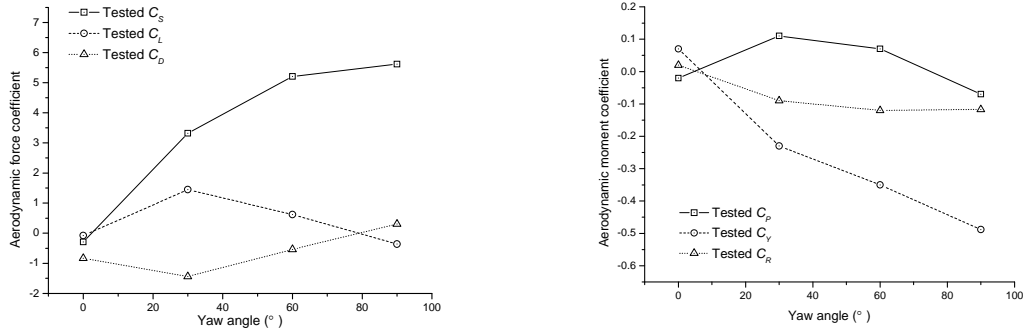


Fig. 4 Aerodynamic coefficients of the lorry

### 3. Numerical simulation of stationary lorry

#### 3.1 Simulation scheme

Owing to the less computation effort of RANS in solving the averaged flow feature, the unsteady RANS method is employed to numerically calculate the flow field around the lorry. The basic ideal behind unsteady RANS is to average the instantaneous flow governing equations in the time domain. After being averaged, the imprmissible flow governing equations become

$$\frac{\partial \bar{u}_i}{\partial x_i} = 0 \quad (5)$$

$$\rho \frac{\partial \bar{u}_i}{\partial t} + \rho \bar{u}_j \frac{\partial \bar{u}_i}{\partial x_j} = -\frac{\partial \bar{p}}{\partial x_i} + \mu \nabla^2 \bar{u}_i - \frac{\partial \overline{\rho u'_i u'_j}}{\partial x_j} \quad (6)$$

where  $t$  is the time;  $x_i$  is the coordinate in the  $i^{\text{th}}$  axis in the Cartesian coordinate system;  $\rho$  and  $\mu$  are the density and dynamic viscosity coefficient of air, respectively;  $u_i$  is the velocity component along the  $x_i$ -axis;  $u'_i$  is the fluctuation part of  $u_i$ ;  $p$  is the pressure; the over bar represents the mean value;  $-\rho u'_i u'_j$  is the so-called Reynolds stress represented by the SST  $k-\omega$  turbulence model in this study. The governing equations are discretized using QUICK scheme based on the finite volume method. SIMPLEC algorithm is employed for the coupling of velocity and pressure. The time integration is performed using the second-order implicit method. The CFD code Fluent is employed to solve the parameters of flow field.

#### 3.2 Computational domain and boundary condition

As shown in Fig. 5, the entire computation domain is a cube enclosed with six outer boundaries:  $b\_left$ ,  $b\_right$ ,  $b\_head$ ,  $b\_tail$ ,  $b\_up$  and  $ground$ . Outer boundary  $b\_left$  is the inflow face where wind blows into the domain.  $b\_right$  is parallel to  $b\_left$  with a offset of  $Dx$ . The  $ground$  represents the place where the lorry stays on.  $b\_up$  is parallel to  $ground$  with a distance of  $Dy$ .  $b\_head$  and  $b\_tail$  are the outer boundaries of the cube with  $b\_head$  near the head of vehicle and  $b\_tail$  near the tail of vehicle. The distance between  $b\_head$  and  $b\_tail$  is  $Dz$ .  $z1$  and  $z2$  are the distances of the

head and tail surfaces of the vehicle to the boundaries  $b_{head}$  and  $b_{tail}$ , respectively. The total size of the domain is:  $Dx = 10L$ ,  $Dy = 6.7H$ , and  $Dz = 15L$  ( $H$ ,  $L$  are the height and length of the vehicle, respectively). When the vehicle stays with its longitudinal axis perpendicular to the upcoming wind direction ( $90^\circ$  yaw angle), the blockage ratio reaches the maximum value compared with other yaw angle cases. At  $90^\circ$  yaw angle,  $z_1$  and  $z_2$  are  $3.5L$  and  $10.5L$ , respectively, and the maximum blockage ratio is about 1.5%.

All boundaries including the six outer boundaries and the surfaces of the vehicle are enforced with mathematic boundary conditions to approximate the real situation.  $b_{left}$  is the source of upcoming wind. A uniform wind velocity of 10m/s, turbulence kinetic energy of 0.05 and special dissipation ratio of 2 are assigned to this boundary. After the flow passes the vehicle, wind blows out of the domain through the outer boundary  $b_{right}$ . Thus,  $b_{right}$  is specified as flow outlet with zero pressure. The outer boundaries  $b_{up}$ ,  $b_{head}$  and  $b_{tail}$  are parallel to the direction of the upcoming wind. The flows at these boundaries are assumed uniform and the gradients of flow variables (including wind velocity and pressure) normal to the boundaries are zero. The flow can not penetrate the ground and the surfaces of lorry, and no-slip wall is assigned to the ground and vehicle surfaces.

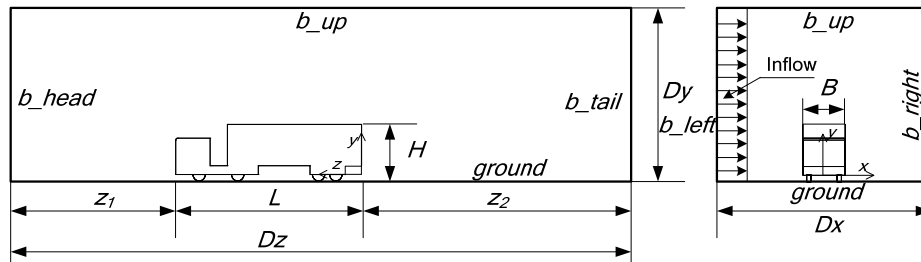


Fig. 5 Computational domain sketch

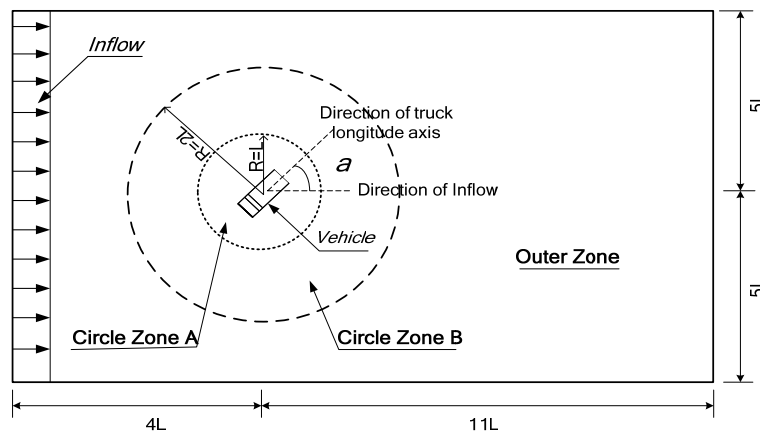


Fig. 6 Schematic diagram of domain decomposition

### 3.3 Domain decomposition and meshing

For the sake of taking into account the variation of yaw angle, the computational domain is decomposed into three sub-domains: Circle Zone A, Circle Zone B and Outer Zone as shown in Fig. 6. Circle Zone A has a geometric shape of cylinder with a radius of  $L$ . It enwraps the vehicle model directly and can be rotated together with the vehicle model as a whole to any yaw angle. Circle Zone B is set outside of Circle Zone A with an outer radius of  $2L$ . It is a transition region between the Circle Zone A and the Outer Zone.

To check the independence of grids, three meshing schemes with different grid sizes are generated. In the three meshing schemes, the grid distributions on vehicle surfaces and the height of the first layer grid near the walls keep consistent, and the grid density in the left flow regions becomes the focus. The height of the first layer grid near the surfaces of vehicle and the ground is  $1 \times 10^{-5}$  m, which ensures that the  $y^+$  of the first layer grid near the walls is below 1 in the simulation. The grid distributions on the surfaces of the vehicle are shown in Fig. 7. Totally about 56 thousand grids are used for the vehicle surfaces. Meshing scheme 1 is the coarsest case with 3.0 million grids. Its grid distribution is shown in Fig. 8. Meshing scheme 2 has a grid number of 3.8 million, which can be seen in Fig. 9. Meshing scheme 3 is the finest case with 5.4 million grids. It has the densest grid around the vehicle, as shown in Fig. 10.

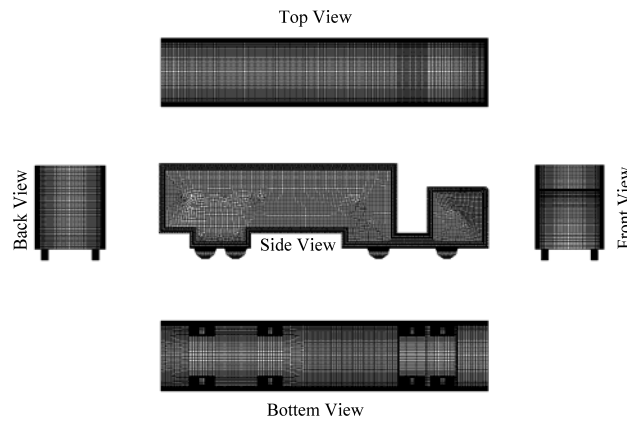


Fig. 7 Grid distributions on vehicle surfaces

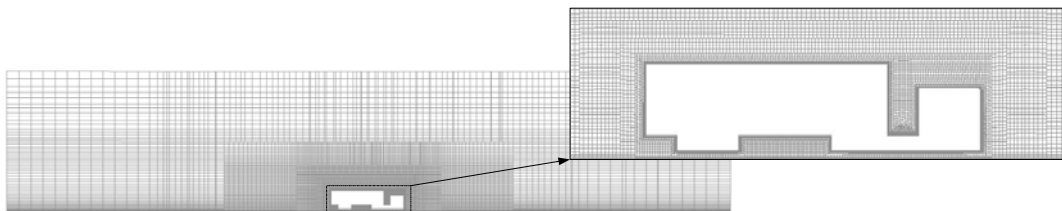


Fig. 8 Grid distributions in meshing scheme 1 (side view)



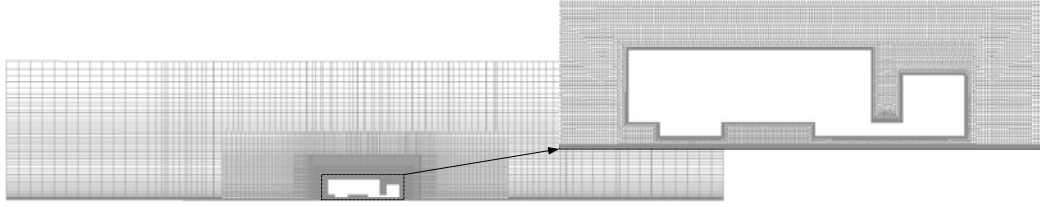


Fig. 9 Grid distributions in meshing scheme 2 (side view)

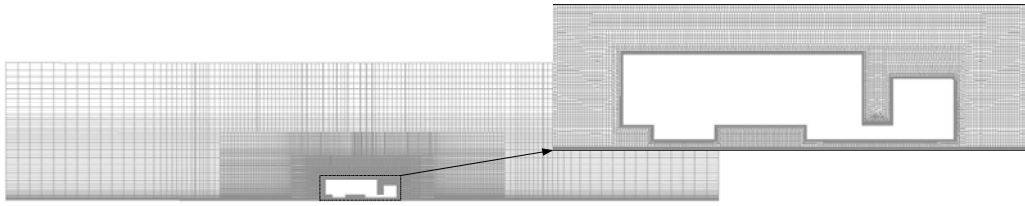


Fig. 10 Grid distributions in meshing scheme 3 (side view)

### 3.4 Time step and length

A dimensional characteristic time  $t^*$  is defined as the ratio of a characteristic length to a characteristic velocity of the flow system. In the cases of a vehicle staying on the ground, wind blows around vehicle, and the characteristic length and characteristic velocity are selected as the width of the vehicle and the upcoming wind velocity. As a result, the characteristic time is expressed as

$$t^* = \frac{B}{U_\infty} \quad (7)$$

where  $B$  and  $U_\infty$  are the width of vehicle and the upcoming wind velocity.

The time step and length for the calculation are set based on  $t^*$ . For the case of  $90^\circ$  yaw angle, two time step  $0.1t^*$  and  $0.05t^*$  are simulated to check the influence of time step on the results. For all the cases, the first  $60t^*$  is treated as a converging process and the corresponding results will not be taken into account. The next  $60t^*$  is accepted as the time length for the normal computational results. The following results including the aerodynamic coefficients, averaging velocity, velocity profile, and pressure coefficient are averaged values on the last  $60t^*$ . The instantaneous stream-lines and vorticity magnitudes are taken from the time at  $120t^*$ .

### 3.5 Numerical simulation results and analyses

#### 3.5.1 Influence of meshing and time step

The three grid systems, meshing scheme 1, meshing scheme 2 and meshing scheme 3, are used to calculate the aerodynamic forces with a time step of  $0.1t^*$ . The mean aerodynamic coefficients are presented in Table 2. It can be seen that the side force coefficient, yawing moment coefficient, rotating moment coefficient keep nearly constant among the three meshing schemes. The lift coefficient, drag coefficient and pitching moment coefficient exhibit a tendency of convergence

with a denser grid. The drag and pitching moment coefficient are nearly constant between meshing scheme 2 and meshing scheme 3. Although the relative differences of lift coefficient and pitching moment coefficient between meshing scheme 2 and meshing scheme 3 are about 11.1% and 16.7% respectively, the corresponding absolute differences are only 0.009 and 0.003. In view of accuracy, meshing scheme 3 is accepted as the proper meshing scheme. For the finest meshing scheme 3, a time step of  $0.05t^*$  is tried to consider the influence of time step on the aerodynamic coefficients. The simulated aerodynamic coefficients of different time steps can be seen in Table 3. It can be seen that a time step of  $0.1t^*$  is accurate enough compared with a shorter time step.  $0.1t^*$  is selected as the time step used in the computation of aerodynamic forces on stationary vehicles on the ground.

Table 2 Simulated aerodynamic coefficients of the vehicle with different meshing schemes

Meshing	$C_S$	$C_L$	$C_D$	$C_P$	$C_Y$	$C_R$
1	5.022	0.094	0.400	-0.003	-0.595	-0.203
2	5.017	0.072	0.380	-0.021	-0.597	-0.204
3	4.997	0.081	0.383	-0.018	-0.593	-0.203

Table 3 Simulated aerodynamic coefficients of the vehicle with different time steps

Time step	$C_S$	$C_L$	$C_D$	$C_P$	$C_Y$	$C_R$
$0.1t^*$	5.00	0.08	0.38	-0.02	-0.59	-0.23
$0.05t^*$	5.00	0.08	0.39	-0.02	-0.59	-0.23

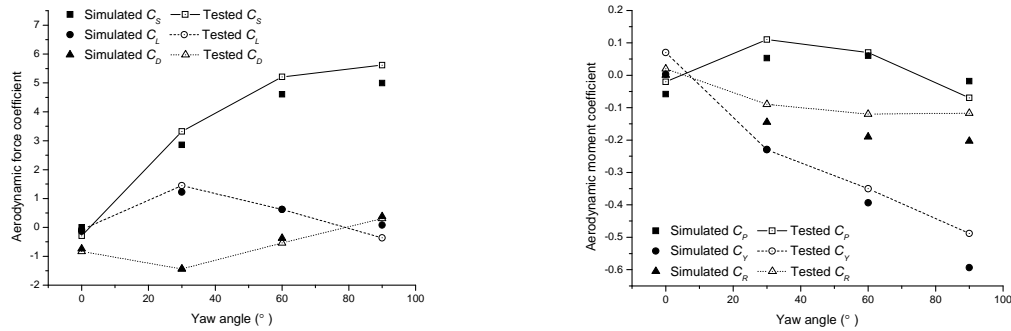


Fig. 11 Aerodynamic coefficient comparison between simulation and test

### 3.5.2 Aerodynamic coefficients with different yaw angles

The flows around the vehicle staying on the ground are numerically calculated for four yaw angles,  $0^\circ$ ,  $30^\circ$ ,  $60^\circ$  and  $90^\circ$ , to consider the influence of upcoming wind direction on the aerodynamic forces of the vehicle. The variations of aerodynamic coefficients with yaw angles are

plotted in Fig. 11. The results of wind tunnel tests are also presented for comparison. It can be seen that the variations of simulated aerodynamic coefficients with yaw angle are similar to the wind tunnel test results. The simulated side coefficients are slightly lower than the measured values, and the largest difference between the simulation and test values is about 0.62. The largest difference of lift coefficient between the simulation and test values is about 0.44. For drag coefficient, a large difference of 0.17 is found. The greatest difference in moment coefficients is about 0.1 at  $90^\circ$  for yawing moment coefficients. As discussed in Section 2, the aerodynamic coefficients from the three tests are different to some extent. Nevertheless, the difference between the simulation and wind tunnel test results presented in this section is much smaller.

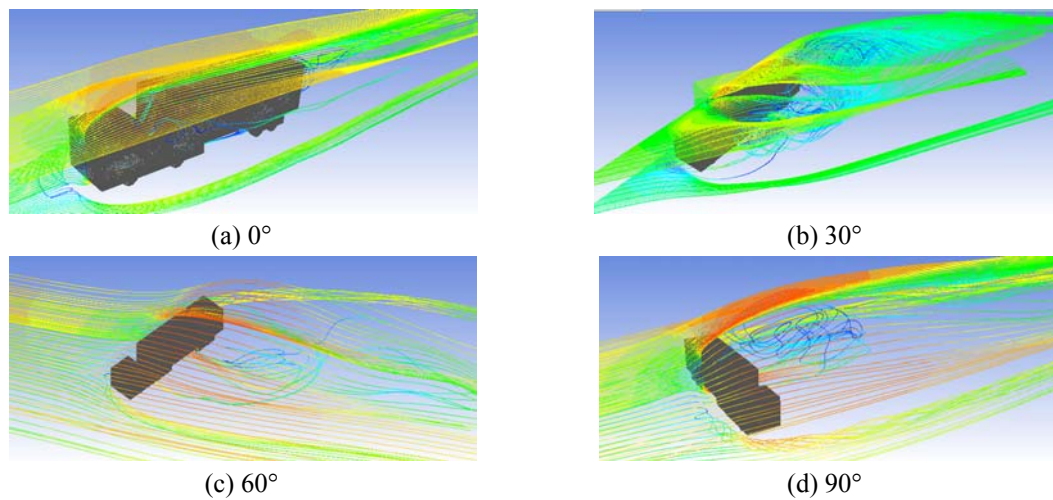


Fig. 12 Instantaneous stream-lines around the lorry at different yaw angles

### 3.5.3 Flow field characteristics

The instantaneous stream-lines around the lorry at different yaw angles are shown in Fig. 12. The flows impact the upwind surfaces of the lorry and form the separated regions around the lorry. At the yaw angle of  $30^\circ$ , the flows reattach to the top surface of the lorry. Clearly, the instantaneous stream-lines around the lorry are different for different yaw angles.

#### (1) Flow features of main sections

The features of flow around the lorry are now presented plane by plane. Two cross sections s1 and s2 in Fig. 2 are selected. s1 is located at the half height of the lorry while s2 is the middle cross section of the trailer. The instantaneous vorticity magnitudes in s1 at different yaw angles are shown in Fig. 13. It can be seen that vortices are generated from the upwind corners of the surfaces. The vorticity distribution for  $0^\circ$  is symmetry about the longitudinal axis of the vehicle. The averaging velocity magnitude contour and streamline of s1 are shown in Fig. 14. With different yaw angles, the flows separate at different locations. At  $0^\circ$  yaw angle, wind blows to the head of the lorry and separate at the both corners of the head surface of the tractor, and a pair of vortices are formed behind the tail surface of the trailer. At  $30^\circ$  yaw angle, the flows separate from the corners between the windward side surface and the tail surface of the trailer, the windward side

surface and the tail surface of the tractor, the head surface of the tractor and the leeward side surface, and the leeward side surface and the head surface of the trailer. Different from  $30^\circ$  yaw angle, the separated flows in the gap between the trailer and tractor do not reattached to the tail surface of the tractor at  $60^\circ$  yaw angle. At  $90^\circ$  yaw angle, the flows separate from the corners between the windward side surface and the tail surface of the trailer, the windward side surface and the head surface of the trailer, and the head surface of the tractor and the windward side surface of the trailer.

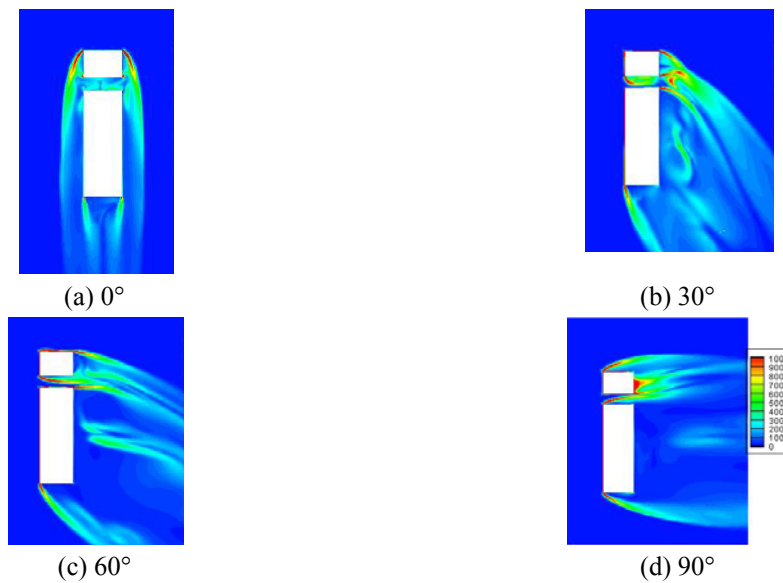


Fig. 13 Instantaneous vorticity magnitude in section s1

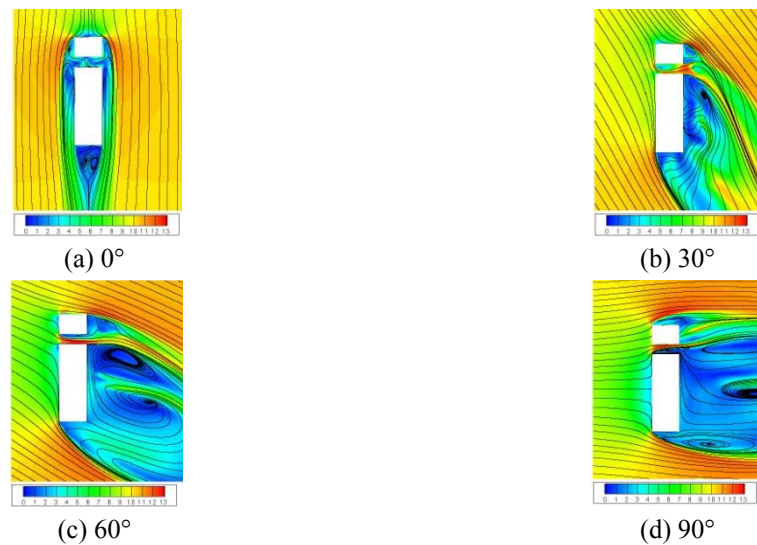


Fig. 14 Averaging velocity magnitude contour and streamline in section s1

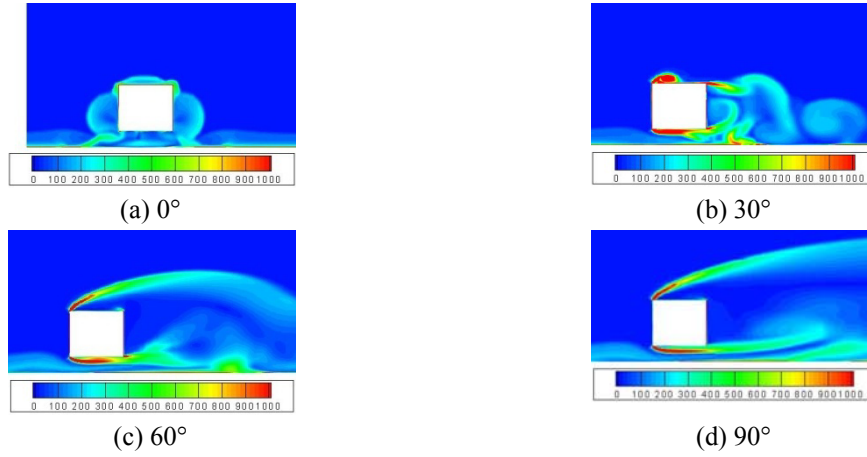


Fig. 15 instantaneous vorticity magnitude in section s2

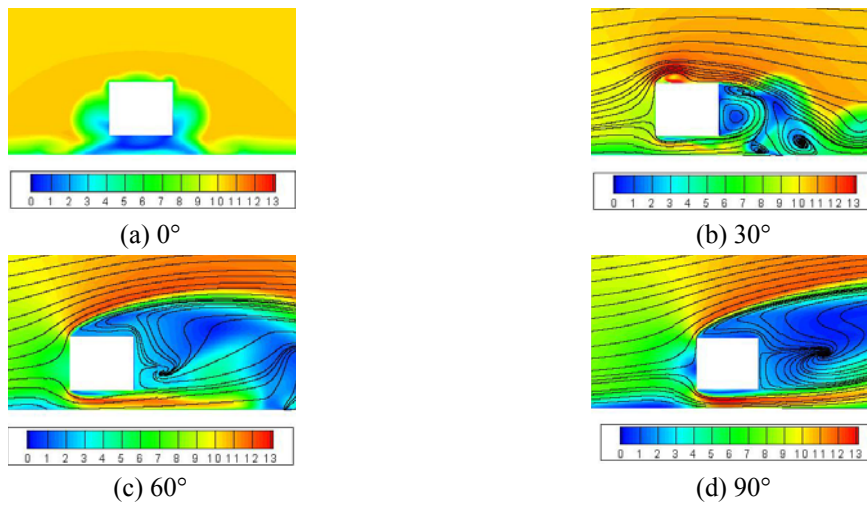


Fig. 16 Averaging velocity magnitude contour and streamline in section s2

The instantaneous vorticity magnitudes in s2 at different yaw angles are shown in Fig. 15. Vortices are generated from the corners of the lorry at the yaw angles of 30°, 60° and 90°. The averaging velocity magnitude contour and streamline of s2 are shown in Fig. 16. For the yaw angles of 60° and 90°, flows separate at the corners between the upwind side surface and the top surface, and the upwind side surface and the bottom surface. For 30°, the flows separate from the corner between the upwind side surface and the top surface first and then reattach to the top surface and finally separate again at the corner between the top surface and the leeward side surface. Several tail vortices are formed behind the leeward side surface.

## (2) Flow features at 30° yaw angle

According to the flow fields shown above, flows around the lorry at 30° yaw angle exhibit different characteristics from those at other yaw angles. The averaging  $z$ -velocity magnitude contour and streamline in section s2 are shown in Fig. 17. The flows separate at the corner between upwind side surface and top surface and then reattach on the top surface. Three vortices are generated in the separation region. These vortices have the velocity in the  $z$  direction (the direction perpendicular to the plane). Thus, they move along  $z$ -direction. After separating at the corner between top surface and leeward side surface and the corner between leeward side surface and bottom surface, two vortices are formed behind the leeward side surface. However, these two vortices have low velocity in the  $z$ -direction. Fig. 18 shows the surface averaging shear stress distributions, which are used to illustrate the surface flow feature. On the windward side surface of the trailer, the reattachment line along the  $y$ -direction illustrates a separating phenomenon emerging there. In the wind direction of the top surface of the trailer, a reattached line, a separating line and a reattached line emerge sequentially which correspond to the flow separating region on the top surface in Fig. 17. The three characteristic flow lines were also reported in the experiments of Coleman and Baker (1990). On the leeward side surface, a separating line is formed, which corresponds to the intersection line between the two vortices behind the leeward surface in Fig. 17.

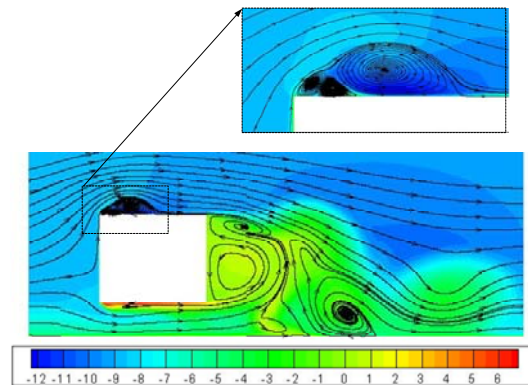


Fig. 17 Averaging  $z$ -velocity magnitude contour and streamline in section s2

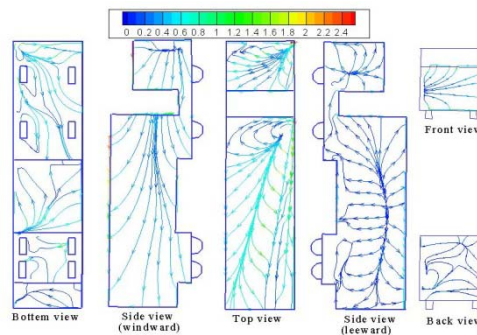


Fig. 18 Averaging shear-stresses on the surface of the lorry

### 3.5.4 Pressure distributions on surfaces

The pressure coefficients (defined as the ratio of measured pressure to the dynamic pressure) over the surfaces of the lorry are viewed from different directions in Fig. 19. The position with a pressure coefficient of 1.0 means a stagnation point. From  $0^\circ$  to  $90^\circ$ , the stagnation points move from the head surface of the tractor to the upwind side surface. The pressures on the upwind surfaces are positive while negative on other surfaces. At  $0^\circ$  yaw angle, the pressure distributions on the two side surfaces are well symmetry. The pressure coefficient is about -0.5 on the tractor surfaces and about -0.1 on the trailer surfaces. At  $30^\circ$  yaw angle, the maximum pressure coefficient on the windward surface is about 0.5. The pressure coefficients on the leeward side surface are negative with an average value about -0.5. At  $60^\circ$  yaw angle, the maximum pressure coefficient on the wind ward surface is about 1.0. The pressure coefficients on the leeward side surface are negative with an average value about -0.5. At  $90^\circ$  yaw angle, the maximum pressure coefficient on the windward side surface is about 1.0. The pressure coefficients on the leeward side surface are negative with an average value about -0.4. From  $0^\circ$  to  $30^\circ$ , the positive pressures on the windward side increase, and the negative pressures on the leeward side surface become lower. From  $30^\circ$  to  $60^\circ$ , the positive pressures on the windward surface continue increasing and the distribution area become larger, and the negative pressures on the leeward surface remain similar. From  $60^\circ$  to  $90^\circ$ , the maximum positive pressure on the windward keeps constant and the distribution area of the large pressure increases while the negative pressure on the leeward surface keeps stable. Due to the interference of vehicle wheels, the pressure distributions on the bottom surfaces of the vehicle are much more complex than other surfaces. From  $0^\circ$  to  $90^\circ$ , the pressure on the bottom surface tends to be lower. A very low negative pressure about -1.5 is distributed on the top surface of the vehicle, which leads to a relative large lift coefficient at  $30^\circ$  yaw angle.

Coleman and Baker (1990) measured the pressure coefficients over the surfaces of a similar lorry. The measured results are taken to compare with the simulation results obtained from this study. Tables 4 to 7 show the comparison of surface pressure coefficients between the simulation and wind tunnel test. The locations of the selected pressure coefficients for comparison are on the top surface (points T11 – T34), upwind side surface (points U11 – U34) and downwind side surface (points D11 – D34) of the trailer as shown in Fig. 20. At  $0^\circ$  yaw angle, all the three surfaces (top, upwind and downwind surfaces) are included in the flow separation regions. Very low negative pressure coefficients are detected in both the simulation and test. The maximum differences between the simulation and test values range from -0.08 to 0.05.

At  $30^\circ$  yaw angle, very low negative pressure coefficients are measured at the tail points which are not found in the simulated results. The maximum differences between the simulation and test values are 0.19 and -0.17 on the top surface. The corresponding relative differences are about -22.6% and 27.9%.

At  $60^\circ$  yaw angle, the pressure coefficients on the upwind surface are positive and those on other two surfaces are negative, which exhibit in both the simulation and test. The maximum differences between the simulation and test values are 0.28 and -0.11 on the upwind surface.

At  $90^\circ$  yaw angle, the pressure coefficients on the upwind surface are positive and those on other two surfaces are negative, which again exhibit in both the simulation and test. The maximum differences between the simulation and test values are 0.36 on the upwind surface and -0.13 on the top surface.



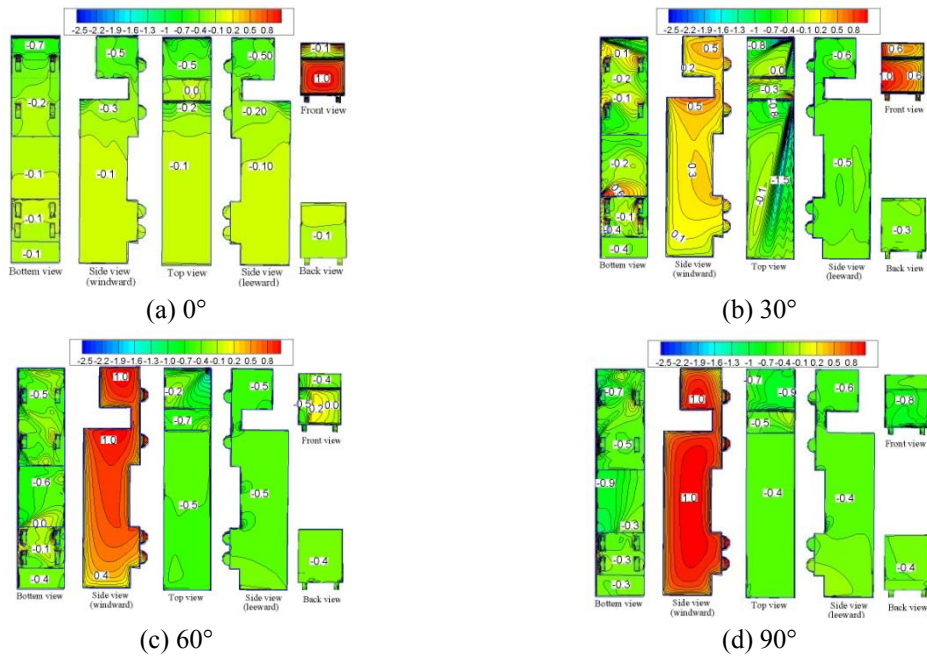


Fig. 19 Pressure distributions on the surfaces of the lorry


	Downwind surface			
	■ D14	■ D13	■ D12	■ D11
	■ D24	■ D23	■ D22	■ D21
	■ D34	■ D33	■ D32	■ D31
Top surface				
	■ T14	■ T13	■ T12	■ T11
	■ T24	■ T23	■ T22	■ T21
	■ T34	■ T33	■ T32	■ T31
Upwind surface				
	■ U14	■ U13	■ U12	■ U11
	■ U24	■ U23	■ U22	■ U21
	■ U34	■ U33	■ U32	■ U31

Fig. 20 Locations of compared pressure coefficients



Table 4 Surface pressure coefficients at 0° yaw angle

(a) Top surface								
Tested value			Simulated value			Difference (simulated value - tested value)		
T11-T14	T21-T24	T31-T34	T11-T14	T21-T24	T31-T34	T11-T14	T21-T24	T31-T34
-0.08	-0.07	-0.07	-0.03	-0.03	-0.03	0.05	0.04	0.04
-0.06	-0.05	-0.06	-0.04	-0.04	-0.04	0.02	0.01	0.02
-0.04	-0.05	-0.05	-0.06	-0.06	-0.06	-0.02	-0.01	-0.01
-0.13	-0.16	-0.14	-0.15	-0.15	-0.13	-0.02	0.01	0.01

(b) Upwind surface								
Tested value			Simulated value			Difference (simulated value - tested value)		
U11-U14	U21-U24	U31-U34	U11-U14	U21-U24	U31-U34	U11-U14	U21-U24	U31-U34
-0.07	-0.09	-0.10	-0.04	-0.05	-0.07	0.03	0.04	0.03
-0.05	-0.05	-0.09	-0.05	-0.04	-0.06	0.00	0.01	0.03
-0.05	-0.04	-0.07	-0.06	-0.06	-0.08	-0.01	-0.02	-0.01
-0.11	-0.12	-0.19	-0.14	-0.15	-0.19	-0.03	-0.03	0.00

(c) Downwind surface								
Tested value			Simulated value			Difference (simulated value - tested value)		
D11-U14	D21-U24	D31-U34	D11-U14	D21-U24	D31-U34	D11-U14	D21-U24	D31-U34
-0.10	-0.08	-0.07	-0.07	-0.04	-0.04	0.03	0.04	0.03
-0.06	-0.05	-0.05	-0.05	-0.04	-0.04	0.01	0.01	0.01
-0.05	-0.06	-0.05	-0.09	-0.07	-0.08	-0.04	-0.01	-0.03
-0.15	-0.09	-0.16	-0.20	-0.17	-0.13	-0.05	-0.08	0.03

Table 5 Surface pressure coefficients at 30° yaw angle

(a) Top surface								
Tested value			Simulated value			Difference (simulated value - tested value)		
T11-T14	T21-T24	T31-T34	T11-T14	T21-T24	T31-T34	T11-T14	T21-T24	T31-T34
-0.37	-0.61	-0.53	-0.20	-0.78	-0.51	0.17	-0.17	0.02
-0.21	-0.48	-1.06	-0.14	-0.48	-0.90	0.07	0.00	0.16
-0.35	-0.28	-1.48	-0.27	-0.18	-1.53	0.08	0.10	-0.05
-0.77	-0.84	-0.64	-0.59	-0.65	-0.58	0.18	0.19	0.06

(b) Upwind surface								
Tested value			Simulated value			Difference (simulated value - tested value)		
U11-U14	U21-U24	U31-U34	U11-U14	U21-U24	U31-U34	U11-U14	U21-U24	U31-U34
-0.03	-0.03	-0.04	0.08	0.12	0.10	0.11	0.15	0.14
0.10	0.15	0.21	0.10	0.23	0.33	0.00	0.08	0.12
0.11	0.20	0.26	0.09	0.24	0.30	-0.02	0.04	0.04
0.25	0.35	0.39	0.19	0.3	0.36	-0.06	-0.05	-0.03

(c) Downwind surface								
Tested value			Simulated value			Difference (simulated value - tested value)		
D11-U14	D21-U24	D31-U34	D11-U14	D21-U24	D31-U34	D11-U14	D21-U24	D31-U34
-0.40	-0.38	-0.38	-0.43	-0.41	-0.42	-0.03	-0.03	-0.04
-0.48	-0.43	-0.36	-0.49	-0.38	-0.42	-0.01	0.05	-0.06
-0.47	-0.42	-0.42	-0.49	-0.38	-0.42	-0.02	0.04	0.00
-0.56	-0.52	-0.48	-0.48	-0.45	-0.47	0.08	0.07	0.01

Table 6 Surface pressure coefficients at 60° yaw angle

(a) Top surface								
Tested value			Simulated value			Difference (simulated value - tested value)		
T11-T14	T21-T24	T31-T34	T11-T14	T21-T24	T31-T34	T11-T14	T21-T24	T31-T34
-0.60	-0.63	-0.62	-0.49	-0.51	-0.52	0.11	0.12	0.10
-0.71	-0.67	-0.65	-0.51	-0.51	-0.51	0.20	0.16	0.14
-0.66	-0.65	-0.65	-0.49	-0.49	-0.49	0.17	0.16	0.16
-0.62	-0.59	-0.60	-0.47	-0.48	-0.49	0.15	0.11	0.11

(b) Upwind surface								
Tested value			Simulated value			Difference (simulated value - tested value)		
U11-U14	U21-U24	U31-U34	U11-U14	U21-U24	U31-U34	U11-U14	U21-U24	U31-U34
0.22	0.26	0.28	0.42	0.54	0.53	0.20	0.28	0.25
0.48	0.59	0.71	0.53	0.72	0.8	0.05	0.13	0.09
0.56	0.71	0.78	0.58	0.78	0.81	0.02	0.07	0.03
0.85	0.96	0.93	0.74	0.88	0.95	-0.11	-0.08	0.02

(c) Downwind surface								
Tested value			Simulated value			Difference (simulated value - tested value)		
D11-U14	D21-U24	D31-U34	D11-U14	D21-U24	D31-U34	D11-U14	D21-U24	D31-U34
-0.52	-0.53	-0.56	-0.38	-0.41	-0.43	0.14	0.12	0.13
-0.67	-0.64	-0.65	-0.48	-0.46	-0.46	0.19	0.18	0.19
-0.52	-0.65	-0.65	-0.48	-0.46	-0.46	0.04	0.19	0.19
-0.62	-0.62	-0.61	-0.47	-0.46	-0.46	0.15	0.16	0.15

Table 7 Surface pressure coefficients at 90° yaw angle

(a) Top surface								
Tested value			Simulated value			Difference (simulated value - tested value)		
T11-T14	T21-T24	T31-T34	T11-T14	T21-T24	T31-T34	T11-T14	T21-T24	T31-T34
-0.49	-0.31	-0.45	-0.45	-0.44	-0.44	0.04	-0.13	0.01
-0.55	-0.52	-0.50	-0.46	-0.45	-0.45	0.09	0.07	0.05
-0.55	-0.51	-0.51	-0.45	-0.45	-0.45	0.10	0.06	0.06
-0.55	-0.54	-0.54	-0.45	-0.45	-0.45	0.10	0.09	0.09

(b) Upwind surface								
Tested value			Simulated value			Difference (simulated value - tested value)		
U11-U14	U21-U24	U31-U34	U11-U14	U21-U24	U31-U34	U11-U14	U21-U24	U31-U34
0.50	0.58	0.74	0.78	0.94	0.93	0.28	0.36	0.19
0.70	0.82	0.90	0.78	1.00	1.00	0.08	0.18	0.10
0.74	0.85	0.95	0.76	0.98	1.00	0.02	0.13	0.05
0.66	0.71	0.75	0.78	0.93	1.00	0.12	0.22	0.25

(c) Downwind surface								
Tested value			Simulated value			Difference (simulated value - tested value)		
D11-U14	D21-U24	D31-U34	D11-U14	D21-U24	D31-U34	D11-U14	D21-U24	D31-U34
-0.38	-0.36	-0.37	-0.29	-0.34	-0.36	0.09	0.02	0.01
-0.47	-0.44	-0.45	-0.41	-0.40	-0.40	0.06	0.04	0.05
-0.42	-0.51	-0.53	-0.43	-0.42	-0.42	-0.01	0.09	0.11
-0.52	-0.52	-0.51	-0.43	-0.41	-0.42	0.09	0.11	0.09

## 4. Numerical simulation of moving lorry

### 4.1 Simulation scheme

As discussed in Section 1, the difference between the stationary lorry and the moving lorry vehicle is whether the movement of the ground is considered or not. For the stationary vehicle, the ground is fixed but the ground moves with a velocity of  $\mathbf{u}_{gv}$  in the moving vehicle case. The other numerical settings of the moving vehicle case are the same as the stationary case. For comparison, the moving cases of the lorry with yaw angles of  $0^\circ$ ,  $30^\circ$  and  $60^\circ$  are simulated.

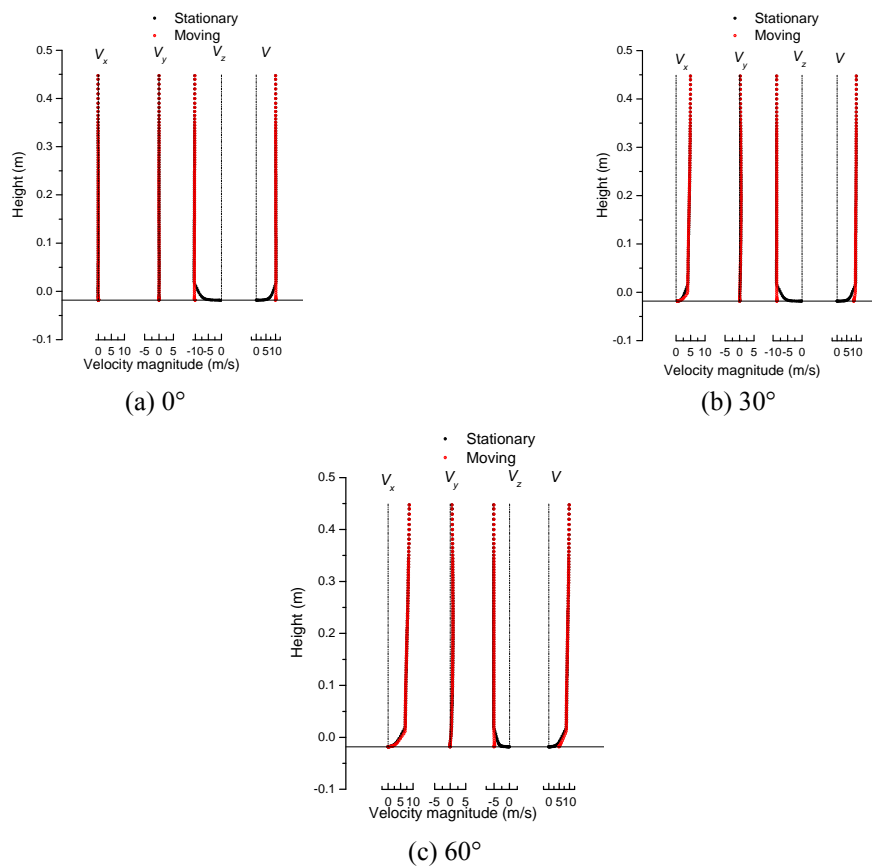


Fig. 21 Velocity profiles at the upcoming locations

### 4.2 Flow field characteristics

Fig. 21 shows the velocity profiles at the position 2.5B away from the longitudinal line of the lorry in the s1 cross section. The flow is not disturbed by the lorry. The difference between the stationary modeling and the moving modeling is found mainly on the velocity  $v_z$  (the velocity component in the longitudinal direction of the lorry) and the total velocity  $v$ . In the  $z$  direction, a

boundary layer with a height about 0.0385 m emerges in the stationary modeling, which does not appear in the moving ground case. From  $0^\circ$  to  $60^\circ$ , the z-velocity components become lower, and the contribution of the z-velocity to the total velocity become lower as well. Thus, the difference in the profiles of total velocity between the stationary and moving vehicle cases become smaller and smaller from  $0^\circ$  to  $60^\circ$ . In other words, the heights of boundary layers tend to be coincident between the stationary and moving modeling from  $0^\circ$  to  $60^\circ$ . The velocity profiles in the s1 cross section are shown in Fig. 22. From  $0^\circ$  to  $60^\circ$ , the differences in the profiles of velocity between the stationary modeling and moving modeling become smaller from  $0^\circ$  to  $60^\circ$ . Although the upcoming flows have some kind of difference in the low part of velocity profiles between the stationary and moving modeling, the velocity profiles for the vehicle are almost the same.

The s1 cross section is far from the ground compared with the boundary layer of the ground and therefore the flow characteristics in this plane have been influenced slightly by changing ground boundary condition. Take the flow characteristics at the yaw angle of  $30^\circ$  as an example as shown in Fig. 23. There is little difference when comparing the moving modeling with the stationary modeling.

The instantaneous vorticity magnitude and averaged velocity in section s2 are shown in Figs. 24 and 25 respectively. Compared with the corresponding cases in the stationary modeling, it can be seen that influences of the moving ground conditions on the flow are only limited in the low boundary layer near the ground. Such influence becomes weaker and weaker from  $0^\circ$  to  $60^\circ$ .

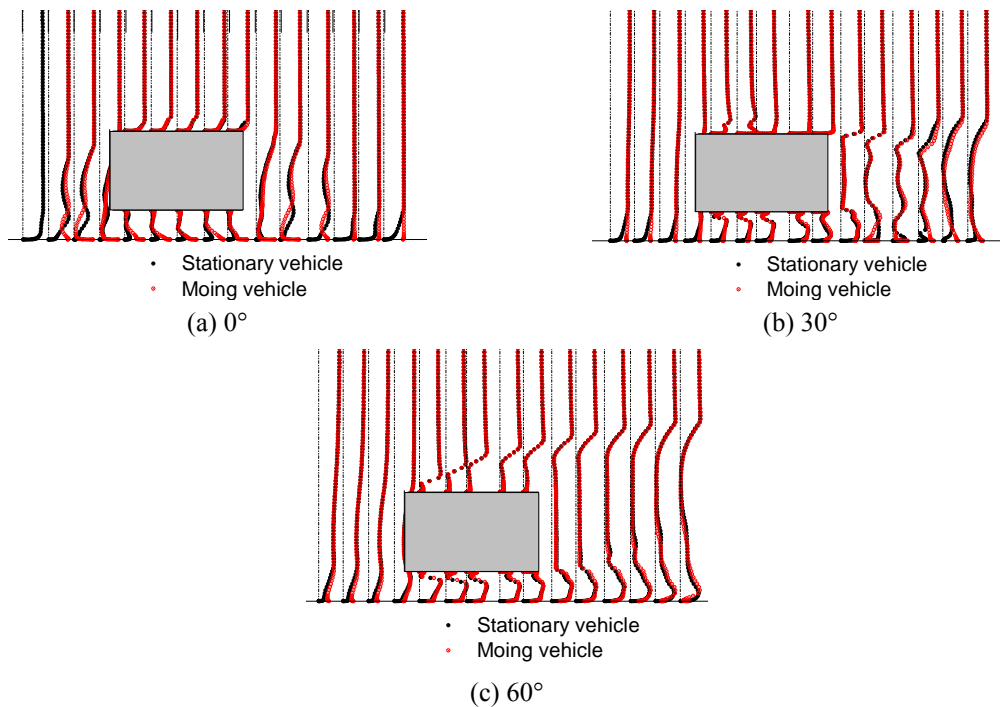


Fig. 22 Velocity profile at the cross sections of the lorry

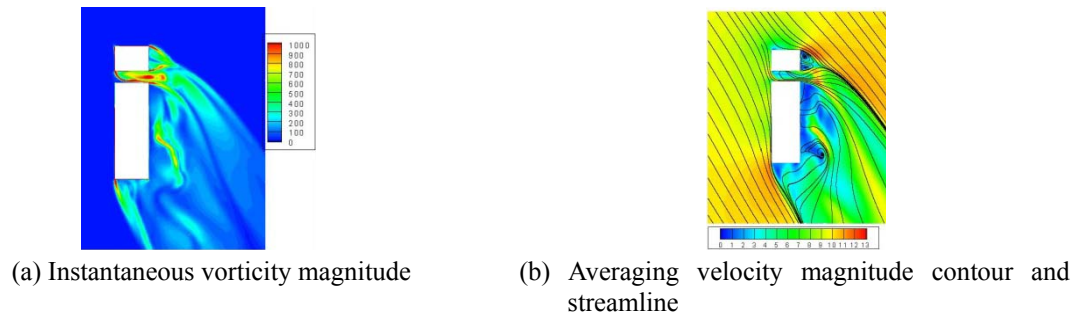


Fig. 23 Flow characteristics in section s1 at 30° yaw angle

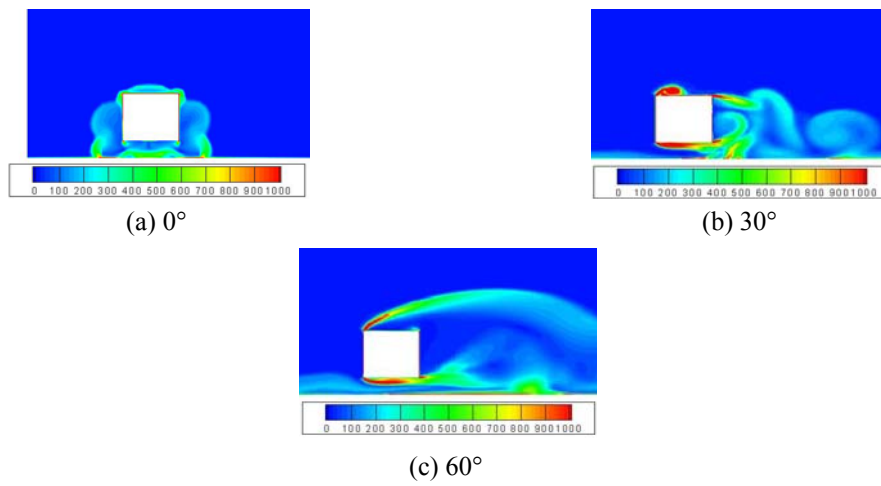


Fig. 24 instantaneous vorticity magnitude in section s1

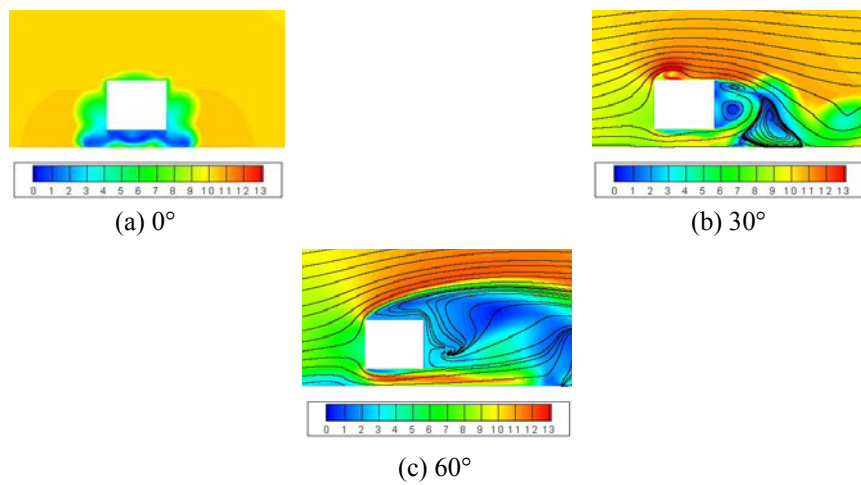


Fig. 25 Averaging velocity magnitude contour and streamline in section s1

### 4.3 Surface flow and pressure distributions

As presented in Section 4.2, the influences of moving ground conditions on the flows near the lorry surface are very small. Therefore, the shear stresses and pressure distribution on the lorry surfaces remain almost unchanged no matter whether the ground is fixed or moving. Fig. 26 shows the surface characteristics of the lorry at 30° yaw angle for the moving ground. It can be seen that there is no significant change compared with the fixed ground case.

### 4.4 Aerodynamic coefficients of moving vehicle

Fig. 27 shows the aerodynamic coefficients of the lorry in both the moving and fixed ground cases. It can be seen that the differences in the aerodynamic coefficients between the two conditions are small. The absolute aerodynamic coefficient values of the moving lorry seem little larger than those of the stationary lorry.

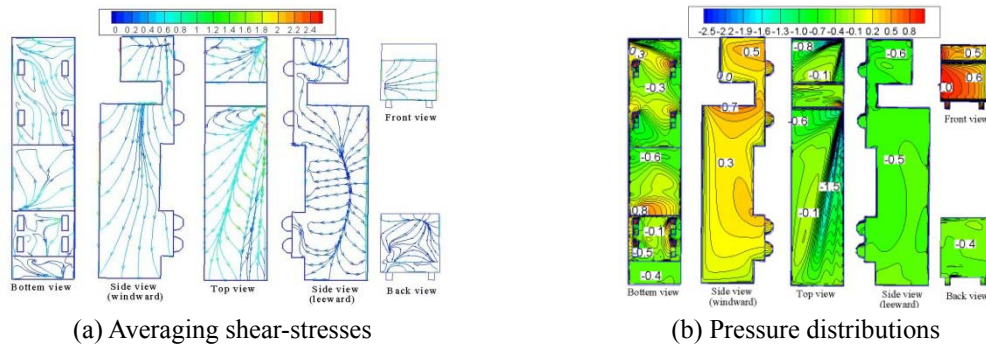


Fig. 26 Surface characteristics of the lorry at 30° yaw angle

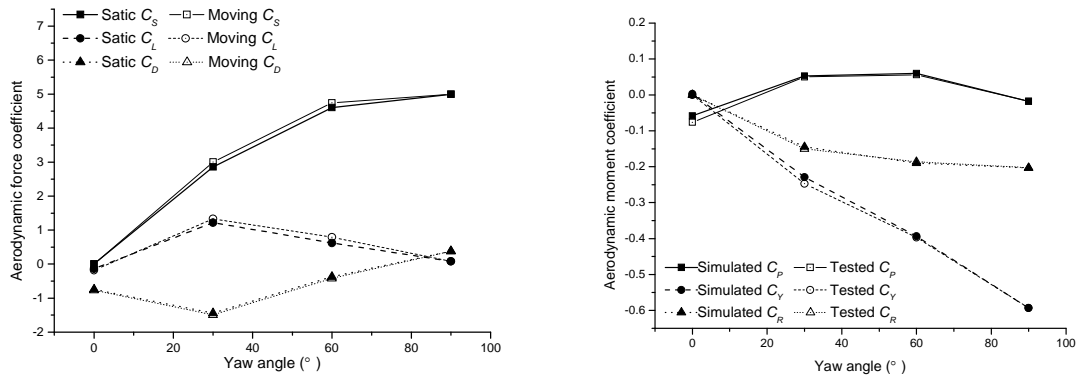


Fig. 27 Comparison of aerodynamic coefficients between stationary and moving ground cases



## 5. Conclusions

This study investigates the aerodynamic characteristics of the high-sided lorry, in which wind tunnel tests are conducted to measure the aerodynamic forces and the CFD simulation with unsteady RANS method is employed to explore the flow field features with and without considering the movement of the lorry. The measured aerodynamic forces agree reasonably well with the previous test results. The numerical aerodynamic coefficients are acceptable after compared with the wind tunnel test results. The flow field features and the surface pressure coefficient distributions on the surfaces of the lorry are simulated. The flows separate at the corners between the surfaces. Different separations are found for different yaw angles. The pressures on the upwind surfaces are positive while negative on other surfaces. Due to the interference of wheels, the pressure distributions on the four bottom surfaces of the vehicle are much more complex than other surfaces. Very low negative pressures are distributed on the top surface of the vehicle. The pressure coefficients at several surface points are compared with the wind tunnel test results. The maximum absolute difference is 0.36 on the windward side surface at 90° yaw angle. The moving ground only impacts the boundary layer wind near the ground. With the increase of the yaw angle, the influences become weak. This could be the reason why the flows appear differently at lower yaw angles in the moving vehicle wind tunnel tests. However, the flow characteristics near the surfaces of the lorry and pressure distributions on the surfaces are only slightly influenced. The corresponding aerodynamic forces on the moving lorry show little difference from those on the stationary lorry.

## Acknowledgements

The authors wish to acknowledge the financial supports from the Research Grants Council of the Hong Kong (PolyU 5311/07E) and The Hong Kong Polytechnic University through a PhD studentship to the first author and a niche area project (PolyU 1-BB20) to the second author.

## References

- Baker, C.J. (1986), "A simplified analysis of various types of wind-induced road vehicle accidents", *J. Wind Eng. Ind. Aerod.*, **22**, 69-85.
- Baker, C.J. (1988), "High sided articulated road vehicles in strong cross wind", *J. Wind Eng. Ind. Aerod.*, **31**, 67-85.
- Baker, C.J. and Reynolds, S. (1992), "Wind-induced accidents of road vehicles", *Accident Anal. Prev.*, **24**(6), 559-575.
- Coleman, S.A. and Baker, C.J. (1990), "High sided road vehicles in cross winds", *J. Wind Eng. Ind. Aerod.*, **36**, 1383-1392.
- Coleman, S.A. and Baker, C.J. (1992), 'The reduction of accident risk for high sided road vehicles in cross winds', *J. Wind Eng. Ind. Aerod.*, **44**(1-3), 2685-2695.
- Coleman, S.A. and Baker, C.J. (1994), "An experimental study of the aerodynamic behaviour of high sided lorries in cross winds", *J. Wind Eng. Ind. Aerod.*, **53**(3), 401-429.
- Gohlke, M. Beaudoin, J. Amielh, M. and Anselmet, F. (2010), "Shape influence on mean forces applied on a ground vehicle under steady cross-wind", *J. Wind Eng. Ind. Aerod.*, **98**(8-9), 386-391.
- Guilmineau, E. and Chometon, F. (2009), "Effect of side wind on a simplified car model: experimental and

- numerical Analysis”, *J. Fluid. Eng. - T ASME*, **131**(2), 021104.
- Han, T. (1989), “Computational analysis of three-dimensional turbulent flow around a bluff body in ground proximity”, *AIJA J.*, **27**(9), 1213-1219.
- Hargreaves, D.M. and Morvan, H.P. (2008), “Initial validation of cross wind effects on a static high-sided vehicle”, *Int. J. CFD Case Studies*, **7**, 17-31.
- Howell, J.P. (1996), “The side load distribution on a rover 800 saloon car under crosswind conditions”, *J. Wind Eng. Ind. Aerod.*, **60**, 139-153.
- Humphreys, N.D. and Baker, C.J. (1992), “Forces on vehicles in cross winds from moving model tests”, *J. Wind Eng. Ind. Aerod.*, **41-44**, 2673-2684.
- Krajnović, S. and Davidson, L. (2003), “Numerical study of the flow around a bus-shaped body”, *J. Fluids Eng. - T ASME*, **125**, 500-509.
- Kim, D.H. Kwon, S.D. Lee, I.K. and Jo, B.W. (2011), “Design criteria of wind barriers for traffic. Part2: decision making process”, *Wind Struct.*, **14**(1), 71-80.
- Kwon, S.D. Kim, D.H. Lee, S.H. and Song H.S. (2011), “Design criteria of wind barriers for traffic. Part1: wind barrier performance”, *Wind Struct.*, **14**(1), 55-70.
- Passmore, M.A. Richardson, S. and Imam, A. (2001), “An experimental study of unsteady vehicle aerodynamics”, *Proceedings of the Institution of Mechanical Engineers, Part D: Journal of Automobile Engineering*.
- Petzäll, J. Torlund, P.Å. Falkmer, T. Albertsson, P. and Björnstig, U. (2008), “Aerodynamic design of high-sided coaches to reduce cross-wind sensitivity, based on wind tunnel tests”, *Int. J. Crashworthiness*, **13**(2), 185-194.
- Proppe, C. and Wetzel, C. (2010), “A probabilistic approach for assessing the crosswind stability of ground vehicles”, *Vehicle Syst. Dyn.*, **48S**, 411-428.
- Sharma, R. Chadwich, D. and Haines, J. (2008), “Aerodynamics of an intercity bus”, *Wind Struct.*, **11**(4), 257-273.
- Snæbjörnsson, J.Th. Baker, C.J. and Sigbjörnsson, R. (2007), “Probabilistic assessment of road vehicle safety in windy environments”, *J. Wind Eng. Ind. Aerod.*, **95**, 1445-1462.
- Tsubokura, M. Kobayashi, T. Nakashima, T. Nouzawa, T. Nakamura, T. Zhang, H. Onishi, K. and Oshima, N. (2009), “Computational visualization of unsteady flow around vehicles using high performance computing”, *Comput. Fluids*, **38**(5), 981-990.
- Xu, Y.L. and Guo, W.H. (2003), “Dynamic behaviour of high-sided road vehicles subject to a sudden crosswind gust”, *Wind Struct.*, **6**(5), 325-346.
- Zhu, L.D. Li, L. Xu, Y.L. and Zhu, Q. (2012), “Wind tunnel investigations of aerodynamic coefficients of road vehicles on bridge deck”, *J. Fluid Struct.*, **30**, 35-50.